Published in final edited form as:
J Nucl Med. 2005 May ; 46(5): 840–849.

Accurate Dosimetry in ^{131}I Radionuclide Therapy Using Patient-Specific, 3-Dimensional Methods for SPECT Reconstruction and Absorbed Dose Calculation

Yuni K. Dewaraja, PhD[1], **Scott J. Wilderman, PhD**[1], **Michael Ljungberg, PhD**[2], **Kenneth F. Koral, PhD**[1], **Kenneth Zasadny, PhD**[3], and **Mark S. Kaminiski, MD**[4]

[1]Division of Nuclear Medicine, Department of Radiology, The University of Michigan Medical Center, Ann Arbor, Michigan

[2]Department of Medical Radiation Physics, University of Lund, Lund, Sweden

[3]Pfizer Global Research and Development, Ann Arbor, Michigan

[4]Division of Hematology and Oncology, Department of Internal Medicine, The University of Michigan Medical Center, Ann Arbor, Michigan

Abstract

^{131}I radionuclide therapy studies have not shown a strong relationship between tumor absorbed dose and response, possibly due to inaccuracies in activity quantification and dose estimation. The goal of this work was to establish the accuracy of ^{131}I activity quantification and absorbed dose estimation when patient-specific, 3-dimensional (3D) methods are used for SPECT reconstruction and for absorbed dose calculation.

Methods—Clinically realistic voxel-phantom simulations were used in the evaluation of activity quantification and dosimetry. SPECT reconstruction was performed using an ordered-subsets expectation maximization (OSEM) algorithm with compensation for scatter, attenuation, and 3D detector response. Based on the SPECT image and a patient-specific density map derived from CT, 3D dosimetry was performed using a newly implemented Monte Carlo code. Dosimetry was evaluated by comparing mean absorbed dose estimates calculated directly from the defined phantom activity map with those calculated from the SPECT image of the phantom. Finally, the 3D methods were applied to a radioimmunotherapy patient, and the mean tumor absorbed dose from the new calculation was compared with that from conventional dosimetry obtained from conjugate-view imaging.

Results—Overall, the accuracy of the SPECT-based absorbed dose estimates in the phantom was >12% for targets down to 16 mL and up to 35% for the smallest 7-mL tumor. To improve accuracy in the smallest tumor, more OSEM iterations may be needed. The relative SD from multiple realizations was <3% for all targets except for the smallest tumor. For the patient, the mean tumor absorbed dose estimate from the new Monte Carlo calculation was 7% higher than that from conventional dosimetry.

Conclusion—For target sizes down to 16 mL, highly accurate and precise dosimetry can be obtained with 3D methods for SPECT reconstruction and absorbed dose estimation. In the future, these methods can be applied to patients to potentially establish correlations between tumor regression and the absorbed dose statistics from 3D dosimetry.

For correspondence or reprints contact: Yuni K Dewaraja, PhD, 3480 Kresge III, University of Michigan Medical Center, 204 Zina Pitcher Pl., Ann Arbor, MI 48109-0552. yuni@umich.edu.

Keywords

3-dimensional dosimetry; radioimmunotherapy; SPECT; Monte Carlo dosimetry; ^{131}I

Radioimmunotherapy (RIT) using ^{131}I is showing great promise in the treatment of non-Hodgkin's lymphoma (NHL) (1–4). High-dose ^{131}I-metaiodobenzylguanidine (^{131}I-MIBG) therapy in combination with myeloblative chemotherapy and hematopoietic stem cell rescue is showing promise in the treatment of children with relapsed or metastatic neuroblastoma (5). The success of RIT and MIBG therapy at our institution as well as at other institutions has renewed interest in accurate ^{131}I absorbed dose estimation. Most clinical ^{131}I radionuclide therapy studies, including a study at our institution involving 47 previously untreated NHL patients, have shown an absent or rather weak relationship between radiation-absorbed dose and tumor response (6–9). To make advances toward individualized treatment planning in radionuclide therapy, it is necessary to establish reliable dose–response relationships for target tissue and dose–toxicity relationships for normal tissue. Typically the dose-limiting organ for RIT has been the bone marrow. However, strategies such as bone marrow reconstitution have been incorporated into radionuclide therapy, including the above ^{131}I-MIBG trial at our institution. With bone marrow reconstitution, as well as with fractionated therapy (10) and with pretargeted therapy (11), larger doses of the radionuclide can be administered before the critical organ tolerance is reached, in which case individualized treatment planning takes on added significance.

In antibody therapy, therapeutic effects from the antibody itself (12) can complicate establishing a correlation between tumor absorbed dose and response. However, it is possible that the lack of better correlation is due to inaccuracies in the absorbed dose estimation methods used thus far. This warrants the effort toward developing and evaluating highly accurate methods for the 2 main steps in tumor and organ dosimetry: (a) activity quantification and (b) absorbed dose calculation. For activity quantification in imaging-derived dosimetry, SPECT is the more robust modality compared with conjugate views. Accurate ^{131}I SPECT quantification is challenging because of the higher energy of the ^{131}I photo-peak (364 keV) and the multiple emissions above this energy. Previous studies by our group showed the large error associated with quantifying ^{131}I activity in small objects when the detector response was not included in the SPECT reconstruction model (13). The source of quantification error was primarily due to the partial-volume effect, defined here as the spread or blurring of regional uptake to surrounding areas due to finite spatial resolution and collimator septal penetration. In ^{131}I RIT, these effects are especially significant because there is considerable uptake in surrounding organs in intravenously administered therapy. To minimize resolution and penetration effects in ^{131}I quantification, researches have developed specialized collimators (14) and incorporated the 3-dimensional (3D) detector response in the system model of the iterative reconstruction (15–17).

The most common approach to internal radionuclide dosimetry has been the MIRD S factor (mean absorbed dose per unit cumulative activity)– based methodology (18). The MIRD S factors were calculated for a Reference Man mathematic phantom, but organ size, shape, and position vary considerably from patient to patient. This approach also precludes calculation of tumor absorbed dose or of dose to normal tissue due to tumor activity. In tumor dosimetry, the nonpenetrating (β) radiation can readily be dealt with by assuming local energy deposition, but there is no simple solution to account for penetrating (photon) radiation. The contribution to tumor absorbed dose from photons in the rest of the body is typically ignored, but for ^{131}I it has been reported that this contributions can be as high as 23% of the total tumor absorbed dose (19). Another limitation of the MIRD methodology is that it provides only the mean absorbed dose to the target. Though these mean dose estimates are quite adequate for diagnostic

applications, with therapeutic applications there is an incentive for greater accuracy and for patient-specific 3D calculation. With 3D dosimetry, apart from the mean absorbed dose to the target, additional statistics such as minimum dose, maximum dose, and dose nonuniformity are available; hence, their correlation to response can also be evaluated. The use of Monte Carlo radiation transport for accurate patient-specific 3D absorbed dose estimation is well accepted (20,21) but has not been common because of limitations in computational power. More recently, a few groups have implemented 3D Monte Carlo dosimetry for radionuclide therapy applications (16,22,23).

The goal of this work was to establish the accuracy of tumor and organ activity quantification and absorbed dose estimation with patient-specific, 3D methods for the SPECT reconstruction and for the absorbed dose calculation. Since SPECT image quality and activity quantification significantly affect the 3D dose calculation, much emphasis was placed on optimizing the reconstruction and quantification procedures. Three-dimensional dosimetry was performed using a newly implemented Monte Carlo algorithm. Initially, clinically realistic simulation studies were used for the quantification and dosimetry evaluations. Finally, to demonstrate clinical applicability, the 3D methods were used with data from a patient treated at our clinic.

MATERIALS AND METHODS

The inputs to the Monte Carlo dose calculation program are the patient's SPECT activity distribution and the CT-derived density map. In our procedure, CT is also used to derive attenuation maps for the SPECT reconstruction and to define target volumes of interest (VOIs) for dosimetry. Typically, in patient imaging, the SPECT and CT acquisitions are performed sequentially; hence, the 2 images must be coregistered. In phantom simulations described here, the SPECT image and the density map are perfectly matched spatially; hence, registration was not needed.

Monte Carlo Simulations to Mimic SPECT Acquisition

The present evaluation of SPECT activity quantification and dosimetry is based on Monte Carlo simulations of the anatomically correct voxel phantom of Zubal et al. (24). The phantom is a 128 × 128 × 246 matrix with a voxel size of 4 mm in all directions. For the present evaluation, a subset of 60 slices in the abdominal region of the phantom was used and 4 spheric-shaped tumors (7, 16, 59, and 135 mL) were defined. The relative activity concentrations for the various structures were defined to reflect a typical situation in RIT imaging of NHL patients. Table 1 gives the day 2 posttracer administration values for the percentage uptake per gram in tumor, organs, and whole body determined by conjugate views and planar imaging of 9 male patients who underwent ^{131}I RIT at our clinic. The tumors in these patients ranged in size from 46 to 888 mL and were located in either the abdomen or the pelvis. The percentage uptake is defined relative to the total activity that was administered and we can expect that the posttherapy values at a specific time point will be very similar to the posttracer values at that time point. Day 2 posttracer values were used because SPECT of RIT patients at our clinic were typically performed at 2 d after therapy. On the basis of the values of Table 1, we assigned the following relative activity concentration values for the phantom: 7-mL tumor, 100; 16-mL tumor, 100; 59-mL tumor, 100; 135-mL tumor, 100; kidney, 80; liver, 28; lung, 28; spleen, 52; blood-pool, 48; rest of the body, 4. The total activity in the camera field of view (FOV) was set to 1 GBq. The activity and density distribution for 2 typical slices of the voxel phantom are shown in Figures 1A and 1B.

Simulation of SPECT projections was performed using the latest version of the SIMIND Monte Carlo code (25), which has been validated for ^{131}I (13). A Picker Prism 3000 SPECT camera was modeled with both a conventional high-energy collimator (HE collimator) used clinically for ^{131}I and a commercial ultra-high-energy collimator (UHE collimator) that minimizes septal

penetration. SPECT simulations used 360°, 60 angles, a 20% photopeak at 364 keV, two 6% adjacent scatter-correction windows, and a 128 × 128 matrix with a pixel size of 4 mm. The distance from the phantom center to the camera was 26 cm.

To generate essentially noise-free projections, 3×10^{10} photons were simulated per projection. The projection data were scaled to 10 million total number of counts, which is typical for patient imaging after the therapy administration of ^{131}I. We generated pseudorandom Poisson distributed projection measurements having mean values corresponding to 10 million total counts, representing typical noise levels for patient imaging. In this way, multiple (twenty) independent noisy projection datasets were generated to obtain a reliable estimate of the accuracy and precision of activity quantification and absorbed dose estimation. The projection datasets were reconstructed as described.

3D SPECT Reconstruction

It is important to optimize the SPECT reconstruction by compensating for the effects that degrade image quality. Reconstruction was performed with an unregularized multiplane (3D) ordered-subsets expectation maximization (OSEM) algorithm that included depth-dependent detector response modeling, nonuniform attenuation correction, scatter correction, and no postfiltering. The 60 SPECT projections were grouped into 6 subsets. For the UHE collimator, the average behavior of the point source response was modeled by a rotationally symmetric gaussian. For the HE collimator, where septal penetration is substantially higher, a rotationally symmetric single exponential was added to the gaussian to model the penetration tails (17). For attenuation correction, the voxel phantom mass density images were converted to maps of linear attenuation coefficients at 364 keV by multiplying each density voxel value by values of the mass attenuation coefficients for water or bone, with 1.2 g/cm^3 used as the threshold density. Scatter correction was performed using the triple-energy window method, which we have used for ^{131}I SPECT in the past (13). The scatter contribution to each projection element was included in the statistical model as an additive term rather than subtracting it from the projections.

SPECT Activity Quantification

To convert SPECT counts to activity we considered 3 calibration geometries: (a) a point source in air, (b) an elliptic tank with uniform activity, and (c) a hot sphere centered in an elliptic tank with background activity. In all cases, the source– detector distance was 26 cm. The elliptic tank was 23 × 31.5 cm and 20.5 cm in height and the hot sphere was 200 mL in volume. For the hot-sphere geometry, the sphere-to-background activity concentration ratio was 5:1. The SIMIND-generated projection data from the calibration experiment were reconstructed using the 3D OSEM reconstruction, which included detector response modeling, scatter correction, and attenuation correction. For each geometry, the counts-to-activity conversion (cps/MBq) was determined by dividing the reconstructed counts within a VOI by the defined activity for that region. For the uniform tank and the hot sphere, the VOI was defined as the physical size of the tank and the sphere, respectively. For the point source, where it is more difficult to define physical size, we investigated using spheric VOIs centered on the centroid of the source with the radius varying from 1 to 4 pixels.

Tumor and organ quantification was performed by summing the reconstructed counts within the target VOI and dividing by the calibration factor. The VOIs were defined to be the actual physical size of the target, which mimicked the situation in our clinical ^{131}I SPECT studies in which the coregistered patient CT was used to define tight tumor boundaries. First, activity quantification was performed using the calibration factor from each of the 3 calibration geometries. On the basis of these initial results, the optimum calibration geometry was selected and used in the rest of the evaluations.

3D Monte Carlo Absorbed Dose Calculation

The Monte Carlo program DPM (*d*ose-*p*lanning *m*ethod) is a voxel-based electron and photon transport program originally written for fast computation of dose in external electron beam radiotherapy (26). DPM has been extensively benchmarked against other Monte Carlo programs and against experimental measurements (27). For the present internal therapy application, the code was modified to use SPECT-based maps of activity instead of external beam sources. Details of this DPM implementation as well as experimental validation by thermoluminescent dosimeter measurement were recently reported (28). As a further validation, ^{131}I S factors from DPM for various organs of the Zubal phantom are compared with S factors from the MIRDOSE program (29) in Table 2. The MIRDOSE S factors correspond to the MIRD Committee's Reference Man phantom. The organs of the Zubal voxel phantom and the Reference Man mathematic phantom differ considerably in mass and geometry. For self-irradiation S factors, where the dose is mostly due to β-particles, the mass difference between the organs of the 2 phantoms can be accounted for by a simple mass weighting. This mass weighting was applied to the self-irradiation S factors for DPM presented in Table 2, and these values are in very good agreement (within 5%) with MIRDOSE S factors. For cross-irradiation S factors, because the dose is mostly due to photons, a simple mass weighting is not applicable and was not used in Table 2. There is considerable difference between the DPM- and MIRDOSE- generated cross-irradiation S factors, but this can be explained based on the fact that the distances between organs in the 2 phantoms are different. The overlap between kidney and liver, which exists in the Zubal phantom, is not modeled in the Reference Man phantom.

The inputs for the DPM dose calculation are the SPECT activity distribution, the mass density image, the photon and electron cutoff energies, and masks defining tumor and organ VOIs. The photon cutoff was set at 4 keV and the electron cutoff was set at 200 keV, since the range of an electron of this energy is much less than the pixel dimension of 4 mm. The output image from DPM was the absorbed dose rate distribution in units of Gy/MBq-s at the single SPECT time point. The mean absorbed dose rate for each predefined tumor and organ was also generated. Because only one SPECT time point was simulated, the conversion from absorbed dose rate to absorbed dose was performed assuming an effective "half-life" equal to the physical half-life of ^{131}I.

Evaluation Procedure

Both SPECT activity quantification and SPECT-based absorbed dose calculation was evaluated (Fig. 2). Quantification was evaluated by comparing the true tumor and organ activities defined for the voxel phantom with those activities calculated from SPECT images of the same phantom. Dosimetry was evaluated by comparing the "true" mean tumor and organ absorbed dose estimates calculated directly from the predefined voxel-phantom activity and density maps (Fig. 2, bottom branch) with those calculated from SPECT images of the same phantom (Fig. 2, top branch). Because effects that degrade SPECT images such as resolution, penetration, scatter, and attenuation were all modeled, this study establishes the accuracy that can be achieved with SPECT-based 3D absorbed dose estimation.

Patient Study

The DPM absorbed dose calculation was applied to one patient in our ^{131}I RIT data archive. The lymphoma patient (no. 76) had been imaged with a SPECT camera equipped with a UHE collimator 44 h after therapy administration of 4 GBq of ^{131}I -tositumomab. All data needed to perform the 3D calculation existed from a previous study. These included the registered SPECT/CT images for a single time point, the CT-based tumor outline, and estimates of tumor and whole-body activity as a function of time from planar imaging at multiple time points. Time–activity curves from planar imaging had to be used to estimate cumulative activity

required for tumor dosimetry because SPECT was performed only at a single time point. This approach assumes that the SPECT activity distribution measured at a single time point remains constant throughout the uptake and clearance kinetics.

DPM yields 2 components for the tumor, the self-irradiation dose rate due to activity originating within the tumor VOI and the rest-of-the-body dose rate due to activity originating outside the tumor VOI. These components were converted from an absorbed dose rate to absorbed dose using the tumor and rest-of-the-body time–activity curves. For the self-irradiation, the time–activity curve came from evaluative (tracer administration) conjugate-view imaging after scaling the ordinate of the curve by the ratio of the therapy-administered activity divided by the tracer-administered activity. The estimate of the whole-body time–activity curve came from evaluative whole-body imaging with the above scaling. A further scaling, based on mass, was applied to the whole-body time–activity curve to account for the fact that the SPECT FOV was only a fraction of the whole-body camera FOV. The tumor time–activity curve was subtracted from the whole-body time–activity curve to yield the rest-of-the-body time–activity curve. Thus, the DPM calculation ignores the contribution to tumor absorbed dose due to activity outside the SPECT camera FOV. However, because the FOV during patient SPECT was selected such that the tumor was around the center of the FOV, we can expect that the contribution to tumor dose from distant out-of-the-FOV photons to be small. The self and rest-of-the-body components of mean tumor absorbed dose from the 3D DPM calculation were compared with the conventional dosimetry results for this patient. The conventional dosimetry results existed from a previous study (30) and were based only on the MIRDOSE program S values and planar imaging results.

RESULTS

Phantom Study

The total reconstructed counts within each target VOI are plotted as a function of the number of iterations in Figure 3. Although convergence is reached rapidly for large organs, convergence for the smallest tumor is not reached even after 100 iterations. Increasing the number of iterations improves recovery of counts but also increases the noise. Noise is not a significant problem in high-count-rate situations such as imaging after the therapy administration of ^{131}I. Therefore, using a large number of iterations to improve activity quantification is justified in the present application, if computationally feasible. Based on these considerations, 60 iterations were used as the stopping point for all reconstructions in the present study. Two typical slices of the voxel-phantom SPECT reconstruction at 60 iterations are shown in Figure 1C. Even at 60 iterations, quantification error will be large for very small tumors, such as the 7-mL tumor in the present study. However, most tumors analyzed in NHL patients are relatively large. In our previous SPECT evaluation of 179 tumors in 47 NHL patients (9), the tumor volumes ranged from 1.2 to 1,231 mL, with a mean of 74 mL. Of these tumors, 72% were >7 mL.

The data from the calibration experiments were also reconstructed using 60 OSEM iterations. The counts-to-activity conversion factor corresponding to the different calibration geometries are compared in Table 3. The calibration factors with the HE collimator are higher than those with the UHE collimator because of the higher sensitivity of the HE collimator. Because of resolution effects, the point source calibration factor increases sharply as the VOI radius is increased from 1 to 2 pixels but approaches a constant value and does not vary as the VOI radius is increased from 3 to 4 pixels. To determine the optimum calibration geometry, we quantified target activity using the point source (with VOI radius at 2 and 4 pixels), sphere, and uniform tank calibration geometries. The results are compared in Table 4, where the error is the percentage difference between the true activity defined in the phantom and the SPECT-derived activity. In almost all cases, quantification accuracy using the sphere-based calibration

is superior to that using the uniform tank calibration. Comparison between quantification results with the sphere calibration and point source calibration do not show that one geometry clearly outperforms the other. However, because the point source calibration factor is highly sensitive to the size of the VOI, we decided to use the sphere-based calibration for the rest of the evaluations in this study.

Using the sphere-based calibration, the tumor and organ VOI counts in the 20 SPECT realizations were quantified (Table 5). The SPECT-derived activity given in Table 5 is the mean value from the multiple realizations. The error is the percentage difference between the true activity defined for the phantom and the SPECT-derived mean activity. The relative SD is determined from the multiple realizations. Overall quantification accuracy is >9% for organs and >10% for tumors except for the smallest tumor, where the error is up to 43%. Two slices of the voxel-phantom SPECT-based absorbed dose-rate distribution are shown in Figure 1D. For the multiple SPECT realizations, mean tumor and organ absorbed dose results are given in Table 6. The SPECT-derived absorbed dose is the mean value from the multiple realizations. The error is the percentage difference between true absorbed dose calculated directly from the defined phantom activity and the SPECT-based mean absorbed dose. The relative SD is determined from the multiple realizations. Overall dosimetry accuracy is >12% for organs and >6% for tumors except for the smallest tumor, where the error is up to 35%. Comparison of results in Table 5 and Table 6 shows that when there is underestimation of SPECT-based target activity, the dosimetry accuracy is somewhat better than the quantification accuracy (for example, for the 16-mL tumor with the HE collimator, activity quantification error is 10% but the dosimetry error is only 6%). This is because some of the counts that spill out of the target, due to resolution effects, and do not contribute to the target activity, can still contribute to the target absorbed dose. For the same reason, when there is an overestimation of SPECT-based target activity, the dosimetry accuracy is somewhat worse than the quantification accuracy.

For a 128 × 128 × 60 matrix, the time to perform all 60 iterations of the 3D OSEM reconstruction was 150 min on a Digital Equipment Corp. Alpha XP 1000 workstation. For this same matrix, the time to generate low-uncertainty DPM absorbed dose distributions simulating 100 million decays was 50 min on the Alpha workstation.

Patient Study

Figure 4 shows a typical slice of the patient SPECT image, CT image, and the corresponding DPM absorbed dose-rate distribution, including the outline of the large abdominal tumor. The tumor absorbed dose rate was converted to absorbed dose using time–activity curves from planar imaging. The differential dose-volume histogram for the tumor, which shows the fraction of voxels receiving a particular absorbed dose, is shown in Figure 5. The nonuniformity of the dose distribution is evident from the histogram. For this tumor, the minimum absorbed dose is 61 cGy, the mean absorbed dose is 554 cGy, and the maximum absorbed dose is 2,115 cGy. The mean tumor absorbed dose calculated by DPM and conventional dosimetry is compared in Table 7. The self-irradiation component from the 2 calculations shows excellent agreement but, compared with DPM, conventional dosimetry significantly underestimates the rest of the body contribution to the tumor absorbed dose in this patient.

DISCUSSION

The number of iterations and the calibration geometry are important considerations in SPECT quantification. Although convergence was not reached for the smallest sphere, even after 60 iterations, 60 iterations is a reasonable choice for our application where the count-rate is high and typical tumor size is relatively large. For our evaluations, we have used a hot sphere– based calibration where the VOI was defined based on physical size, which is consistent with VOI definition for the targets. In past RIT clinical studies, we have used a hot sphere– based

calibration procedure for ^{131}I SPECT quantification (30). In the present work, good activity quantification accuracy and precision were demonstrated for tumor and organ sizes down to 16 mL. Because of the partial-volume effect, quantification accuracy for the smallest 7-mL tumor was poor and needs to be improved, possibly using more iterations. The present results are significantly better than our previously reported SPECT quantification errors of up to 47% for sphere sizes down to 20 mL using a reconstruction model that did not include the 3D detector response. In the present study, good accuracy was achieved for both collimators, indicating that the gaussian model used for the UHE response and the gaussian-plus-exponential model used for the HE response are reasonable. In terms of overall quantification accuracy and precision, one collimator did not clearly outperform the other. Therefore, the higher sensitivity HE collimator is preferred over the UHE collimator. However, this conclusion applies only when the 3D detector response, including geometric and penetration effects, is included in the reconstruction model. Other investigators have used ^{131}I SPECT quantification procedures that are different from ours, and the most recent of these that used 3D reconstruction with detector response modeling are summarized here. In the study by Ljungberg et al., the calibration factor for quantification was determined from simulations with a known activity point source in air and the corresponding counts in the entire camera FOV (16). Accurate activity quantification was reported for the total phantom and for the liver but results for other smaller organs were poor, possibly due to using too few iterations. Another group used a specially designed high-resolution rotating parallel-hole collimator (RPHC) to achieve a SPECT quantification error of only 3%–17% in small tumors (15). The RPHC designed to minimize septal penetration in brain tumor imaging has a small FOV and trades off sensitivity for resolution.

In the patient study, as expected, the self-irradiation component of the tumor absorbed dose calculated by DPM and by the conventional MIRD-based method did not differ significantly. However, the conventional calculation significantly underestimates the rest-of-the-body contribution to tumor absorbed dose. This is because the S factor– based conventional calculation assumes that the activity in the rest of the body is uniformly distributed, whereas, in reality, the distribution is highly nonuniform as is evident in the patient SPECT image. If the tumor is close to a high-uptake organ, the assumption of uniform activity can greatly underestimate the rest-of-the-body contribution. The DPM calculation, based on the patient's measured activity distribution from SPECT, can be significantly more accurate in this case. In Table 7, the rest-of-the-body contribution to tumor absorbed dose determined from DPM was 2.4 times higher than that determined from conventional dosimetry. However, the total tumor absorbed dose calculated by DPM was only 7% higher than that calculated by conventional dosimetry. This difference itself may not justify the additional image acquisitions, registration, and computations involved with carrying out the DPM calculation. However, in studies in which the rest-of-the-body component of tumor dose is a higher fraction of the total tumor dose than that in the present example, we can expect the difference between the 2 calculations to be more significant. We also note that, for most studies in the RIT data archive at our institution, coregistered SPECT/CT images are available since CT-derived attenuation maps were used for SPECT reconstruction. When these images are available, the DPM calculation itself is straightforward, requiring only about 1 h of computation time on a workstation. The justification for the DPM calculation is not only the improved accuracy but also the generation of 3D dose distributions. Apart from the mean absorbed dose, the dose-volume histogram (Fig. 5) provides other statistical information, such as the minimum dose, the maximum dose, and the nonuniformity of the distribution. In the future, our goal is to perform 3D dosimetry for several patients to potentially establish a correlation between tumor regression and these statistics that describe tumor absorbed dose.

The approach of using time–activity curves from planar imaging to estimate cumulative activity has also been used in other SPECT-based dosimetry studies because multiple SPECT acquisitions are typically not available (8,30). A recent study demonstrated the importance of

using multiple 3D image sets to obtain cumulated activity images for 3D dosimetry compared with combining planar imaging with a single 3D image set (31). In future patient studies, acquisition of multiple SPECT time points should be considered. In the present patient example, the SPECT image was used only to obtain the spatial distribution of the radioactivity while, in addition to the kinetic information, the absolute activity level was also determined by conjugate-view imaging. Since it is generally accepted that quantitative SPECT is superior to quantitative conjugate-view imaging, patient dosimetry can be further improved by using the SPECT-derived absolute tumor activity. The procedure for this would be to scale the ordinate of the conjugate-view time–activity curve so as to produce agreement with the total activity measured by the intratherapy SPECT at the single time point of that imaging (30). In a recent phantom study, it was shown that a single quantitative SPECT combined with a series of conjugate-view scans provides substantially improved absorbed dose estimation compared with conjugate-view scans alone (32).

The effect of SPECT/CT misregistration on activity quantification and dosimetry will be investigated in a future study. We can expect that SPECT/CT misregistration is a major source of error in the patient-specific 3D dosimetry calculation because CT-based attenuation maps are used in the reconstruction and CT-based density maps and target outlines are used in the dose calculation. However, if the recently available commercial combined SPECT/CT systems are used, misregistration will be minimized and 3D dosimetry can be performed with greater ease and accuracy. In the future, we will also perform phantom studies to investigate the effect of the limited FOV of the SPECT camera on the target absorbed dose calculation. In the present study, the absorbed dose due to activity outside the FOV was ignored, because SPECT maps were not available for regions outside the FOV. As discussed earlier, we can expect the out-of-the-FOV contribution to target absorbed dose to be small when the FOV is centered on the target.

It is worth noting that the SPECT-based 3D dosimetry patient study of ^{131}I RIT by Sgouros et al. did not yield a statistically significant correlation between tumor shrinkage and tumor absorbed dose mean, maximum, minimum, or uniformity (8). This finding suggests that in these patients the tumor response cannot be based on radiation-absorbed dose alone, possibly due to the therapeutic effects from the antibody itself. The patients in their study had chemotherapy treatment before RIT, whereas we intend to apply our methods to a previously untreated patient group. Also, we have put much emphasis on optimizing the 3D SPECT reconstruction, whereas the reconstruction method used by Sgouros et al. is not evident in their report. Potentially, the difference in the patient group and use of methods established in the present work will lead to a more favorable dose–response correlation.

CONCLUSION

In 3D dosimetry, the SPECT image quality and activity quantification affect the absorbed dose calculation. Therefore, it is important to have an accurate SPECT reconstruction with compensation for scatter, attenuation, and 3D detector response as well as optimum choice of the number of iterations and the activity calibration geometry. Using a 3D OSEM reconstruction with compensation for these effects, for target sizes down to 16 mL, highly accurate (error < 12%) and precise (SD < 3%) dosimetry results were achieved from a 3D Monte Carlo calculation. This work establishes the accuracy of SPECT-based 3D absorbed dose estimation because the evaluation compared SPECT-based absorbed dose estimates with the absorbed dose calculated directly from the defined phantom activity distribution. The simulation studies were clinically realistic with the targets in the voxel phantom varying in location, size, shape, and relative activity, but the effects of SPECT/CT misregistration were not considered. The 3D methods for SPECT reconstruction and absorbed dose calculation are readily applicable to clinical studies as was demonstrated here for one RIT patient. The mean

tumor absorbed dose for this patient with the new DPM calculation was 7% higher than the results of conventional dosimetry due to potentially more accurate calculation of the rest-of-the-body contribution to tumor dose. The justification for patient-specific 3D dosimetry is not only the improved accuracy but also the generation of other tumor dose statistics such as the minimum and maximum dose and the dose nonuniformity.

Acknowledgments

This work was supported by grants R01 EB001994 and R01 CA87955 awarded by the National Institutes of Health, U.S. Department of Health and Human Services, and by a grant from the Swedish Cancer Foundation. Computing resources provided by the National Partnership for Advanced Computational Infrastructure at the San Diego Supercomputer Center by National Science Foundation cooperative agreement ACI-9619020 are acknowledged. The contents of the paper are solely the responsibility of the authors and do not necessarily represent the official views of the funding agencies.

REFERENCES

1. Press O, Early J, Appelbaum F, et al. Phase II trial of I-131 B1 (anti-CD20) antibody therapy with autologous stem cell transplantation for relapsed B-cell lymphomas. Lancet 1995;346:336–340. [PubMed: 7623531]
2. Kaminski MS, Zasadny KR, Francis IR. Iodine-131-anti B1 radioimmunotherapy for B-cell lymphoma. J Clin Oncol 1996;14:1974–1981. [PubMed: 8683227]
3. DeNardo GL, Lamborn KR, Goldstein DS, Kroger LA, DeNardo SJ. Increased survival associated with radiolabeled lym-1 therapy for non-Hodgkin's lymphoma and chronic lymphocytic leukemia. Cancer 1997;80:2706–2711. [PubMed: 9406728]
4. Kaminski MS, Tuck M, Estes J, et al. I-131 tositumomab therapy as initial treatment for follicular lymphoma. N Engl J Med 2005;352:441–449. [PubMed: 15689582]
5. Yanik GA, Levine JE, Matthay KK, et al. Pilot study of iodine-131-metaiodobenzylguanidine in combination with myeloablative chemotherapy and autologous stem cell support for the treatment of neuroblastoma. J Clin Oncol 2002;20:2142–2149. [PubMed: 11956276]
6. Matthay KK, Huberty JP, Harrner RS, et al. Efficacy and safety of I-131 metaiodobenzylguanidine therapy for patients with refractory neuroblastoma. J Nucl Biol Med 1991;35:244–247. [PubMed: 1823827]
7. DeNardo GL, DeNardo SJ, Shen S, et al. Factors affecting 131-I-Lym-1 pharmacokinetics and radiation dosimetry in patients with non-Hodgkin's lymphoma and chronic lymphocytic leukemia. J Nucl Med 1999;40:1317–1326. [PubMed: 10450684]
8. Sgouros G, Shannon S, Ballangrud AM, et al. Patient specific, 3-dimensional dosimetry in non-Hodgkin's lymphoma patients treated with ^{131}I-anti-B1 antibody: assessment of tumor dose-response. J Nucl Med 2003;44:260–268. [PubMed: 12571219]
9. Koral KF, Dewaraja Y, Li J, et al. Update on hybrid conjugate-view SPECT tumor dosimetry and response in ^{131}I-tositumomab therapy of previously untreated lymphoma patients. J Nucl Med 2003;44:457–464. [PubMed: 12621015]
10. DeNardo GL, DeNardo SJ, Goldstein DS, et al. Maximum tolerated dose, toxicity and efficacy of I-131-Lym-1 antibody for fractionated radioimmunotherapy of non-Hodgkin's lymphoma. J Clin Oncol 1998;16:3246–3256. [PubMed: 9779698]
11. Weiden PL, Breitz HB. Pretargeted radioimmunotherapy for treatment of non-Hodgkin's lymphoma. Clin Rev Oncol Hematol 2001;40:37–51.
12. Davis TA, Kaminski MS, Leonard JP, et al. Results of a randomized trial of Bexxar (tositumomab and I 131 tositumomab) vs unlabeled tositumomab in patients with relapsed or refractory low grade or transformed non-Hodgkin's lymphoma [abstract]. Blood 2001;98:843.
13. Dewaraja YK, Ljungberg M, Koral KF. Accuracy of I-131 tumor quantification in radioimmunotherapy using SPECT imaging with an ultra-high-energy collimator: Monte Carlo study. J Nucl Med 2000;41:1760–1767. [PubMed: 11038009]

14. Smith MF, Gilland DR, Coleman RE, Jaszczak RJ. Quantitative imaging of I-131 distributions in brain tumors with pinhole SPECT: a phantom study. J Nucl Med 1998;39:856–864. [PubMed: 9591589]
15. Gonzalez Trotter DE, Jaszczak RJ, Bowsher JE, Akabani G, Greer KL. High resolution absolute SPECT quantitation for I-131 distributions used in the treatment of lymphoma: a phantom study. IEEE Trans Nucl Sci 2001;48:707–714.
16. Ljungberg M, Sjogreen K, Liu X, Frey E, Dewaraja YK, Strand S. A three dimensional absorbed dose calculation method based on quantitative SPECT for radionuclide therapy: evaluation for I-131 using Monte Carlo simulation. J Nucl Med 2002;43:1101–1109. [PubMed: 12163637]
17. Koral KF, Yendiki A, Lin Q, Dewaraja YK, Fessler JA. Determining total I-131 activity within a VOI using SPECT, a UHE collimator, OSEM and a constant conversion factor. IEEE Trans Nucl Sci 2004;51:611–618.
18. Loevinger, R.; Budinger, TF.; Watson, EE. MIRD Primer. Reston, VA: Society of Nuclear Medicine; 1999. p. 5-6.
19. Johnson TK, Colby SB. Photon contribution to tumor dose from considerations of I-131 radiolabeled antibody uptake in liver, spleen and whole body. Med Phys 1993;6:1667–1674. [PubMed: 8309439]
20. Stabin MG. Internal dosimetry in the use of radiopharmaceuticals in therapy: science at a crossroads? Cancer Biother Radiopharm 1999;14:81–89. [PubMed: 10850291]
21. Zanzonico PB. Internal radionuclide radiation dosimetry: a review of basic concepts and recent developments. J Nucl Med 2000;41:297–308. [PubMed: 10688115]
22. Furhang EE, Chui CS, Kolbert KS, et al. Implementation of Monte Carlo dosimetry method for patient-specific internal emitter therapy. Med Phys 1997;24:1163–1172. [PubMed: 9243479]
23. Yoriyaz H, Stabin MG, dos Santos A. Monte Carlo MCNP-4B-based absorbed dose distribution estimates for patient-specific dosimetry. J Nucl Med 2001;42:662–669. [PubMed: 11337557]
24. Zubal IG, Harrell CR, Smith EO, Rattner Z, Gindi G, Hoffer PB. Computerized three-dimensional segmented human anatomy. Med Phys 1994;21:299–302. [PubMed: 8177164]
25. Ljungberg, M.; Larsson, A.; Johansson, L. A new collimator simulation in SIMIND based on the Delta scattering technique; Conference Record: IEEE Nuclear Science Symposium and Medical Imaging Conference; October 16–22, 2004; Rome, Italy.
26. Sempau J, Wilderman S, Bielajew AF. DPM, a fast, accurate Monte Carlo code optimized for photon and electron radiotherapy treatment planning dose calculations. Phys Med Biol 2000;45:2263–2291. [PubMed: 10958194]
27. Chetty IJ, Moran JM, Nurushev DL, et al. Experimental validation of the DPM Monte Carlo code using minimally scattered electron beams in heterogeneous media. Phys Med Biol 2002;47:1837–1851. [PubMed: 12108770]
28. Wilderman, SJ.; Gunnett, RB.; Kearfott, KJ.; Dewaraja, YK. Fast CT/SPECT derived 3D Monte Carlo dose computations for I-131 internal emitter therapy; Conference Record: IEEE Nuclear Science Symposium and Medical Imaging Conference; October 16–22, 2004; Rome, Italy.
29. Stabin M. MIRDOSE: personal computer software for internal dose assessment in nuclear medicine. J Nucl Med 1996;37:538–546. [PubMed: 8772664]
30. Koral KF, Dewaraja Y, Li J, et al. Initial results for hybrid SPECT-conjugate-view tumor dosimetry in ^{131}I-anti-B antibody therapy of previously untreated patients with lymphoma. J Nucl Med 2000;41:1579–1586. [PubMed: 10994741]
31. Sgouros G, Kolbert KS, Sheikh A, et al. Patient specific dosimetry for ^{131}I thyroid cancer therapy using ^{124}I PET and 3-dimensional-internal dosimetry (3D-ID) software. J Nucl Med 2004;45:1366–1372. [PubMed: 15299063]
32. Frey EC, He B, Sgouros G, et al. Comparison of planar, quantitative SPECT, and combined planar-quantitative SPECT organ residence time estimation methods for targeted radionuclide therapy dosimetry [abstract]. J Nucl Med 2004;45(suppl):46P.

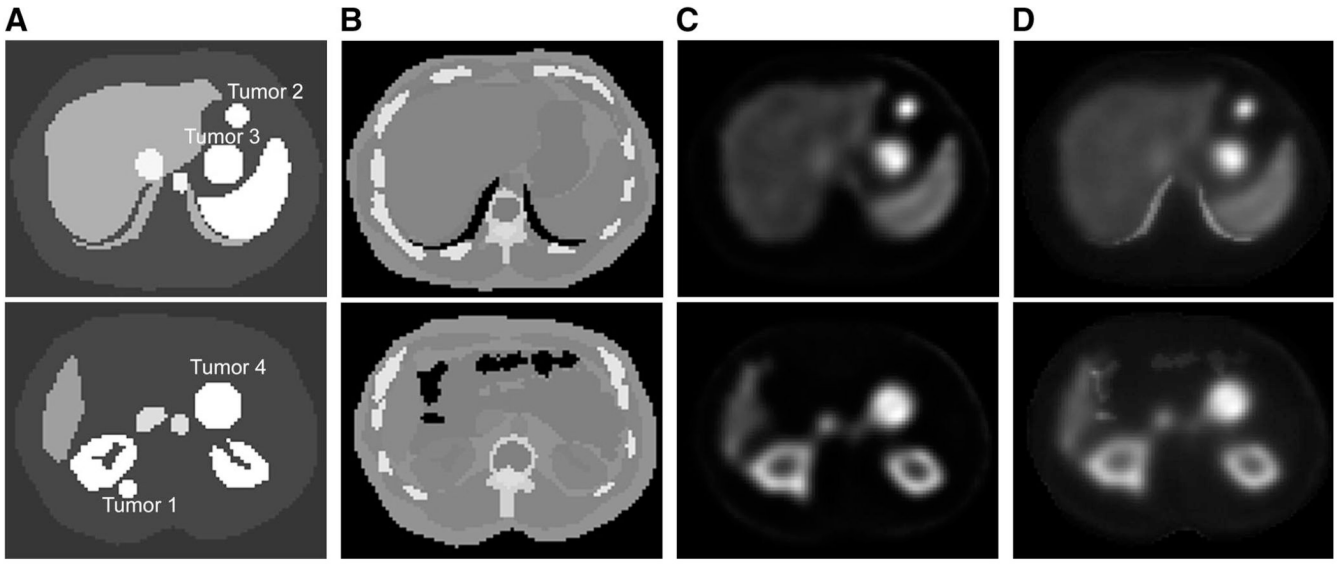

FIGURE 1.
Two typical slices of voxel phantom show superimposed tumors. (A) Defined activity map. (B) Defined density map. (C) SPECT image. (D) Absorbed dose-rate map.

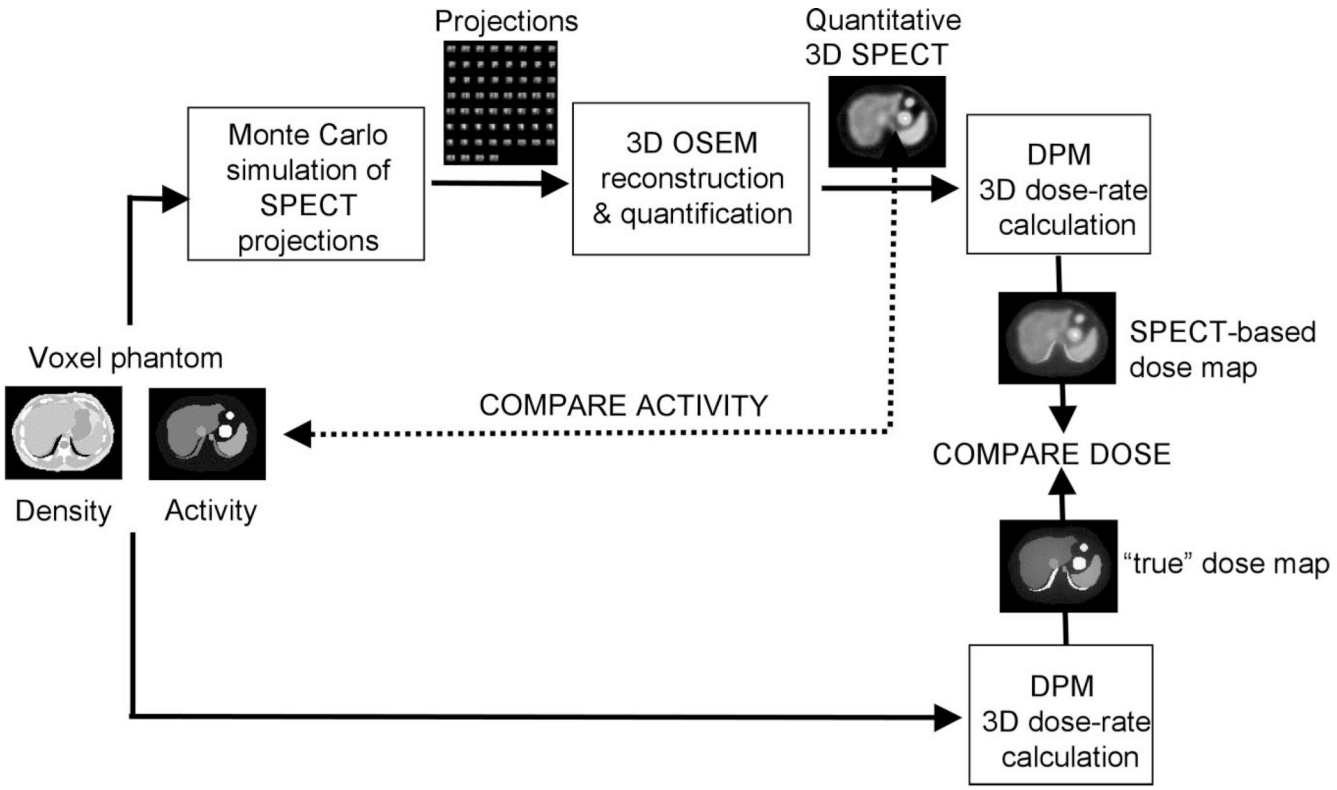

FIGURE 2.
Evaluation procedure.

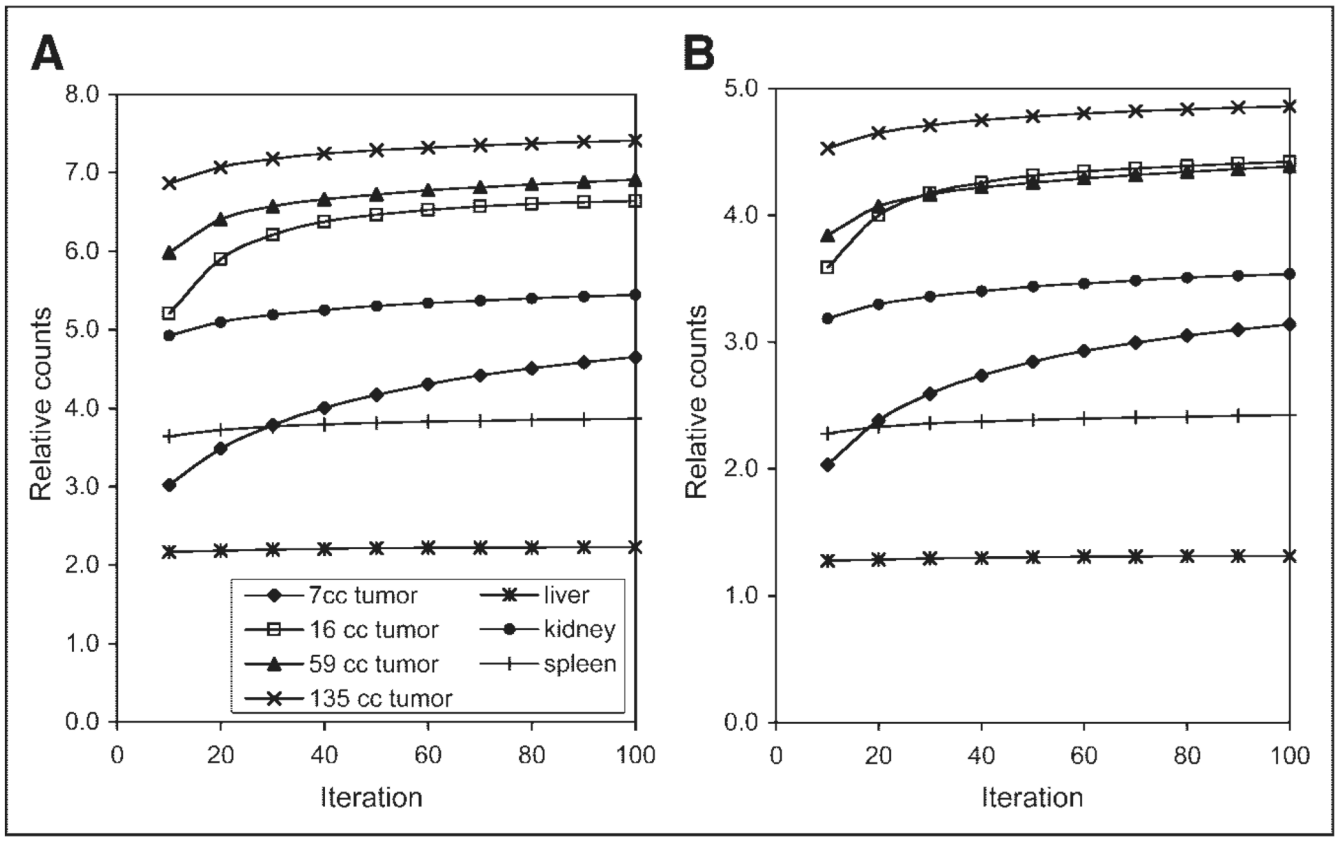

FIGURE 3.
Counts in target VOI plotted as function of iteration number for HE collimator (A) and UHE collimator (B).

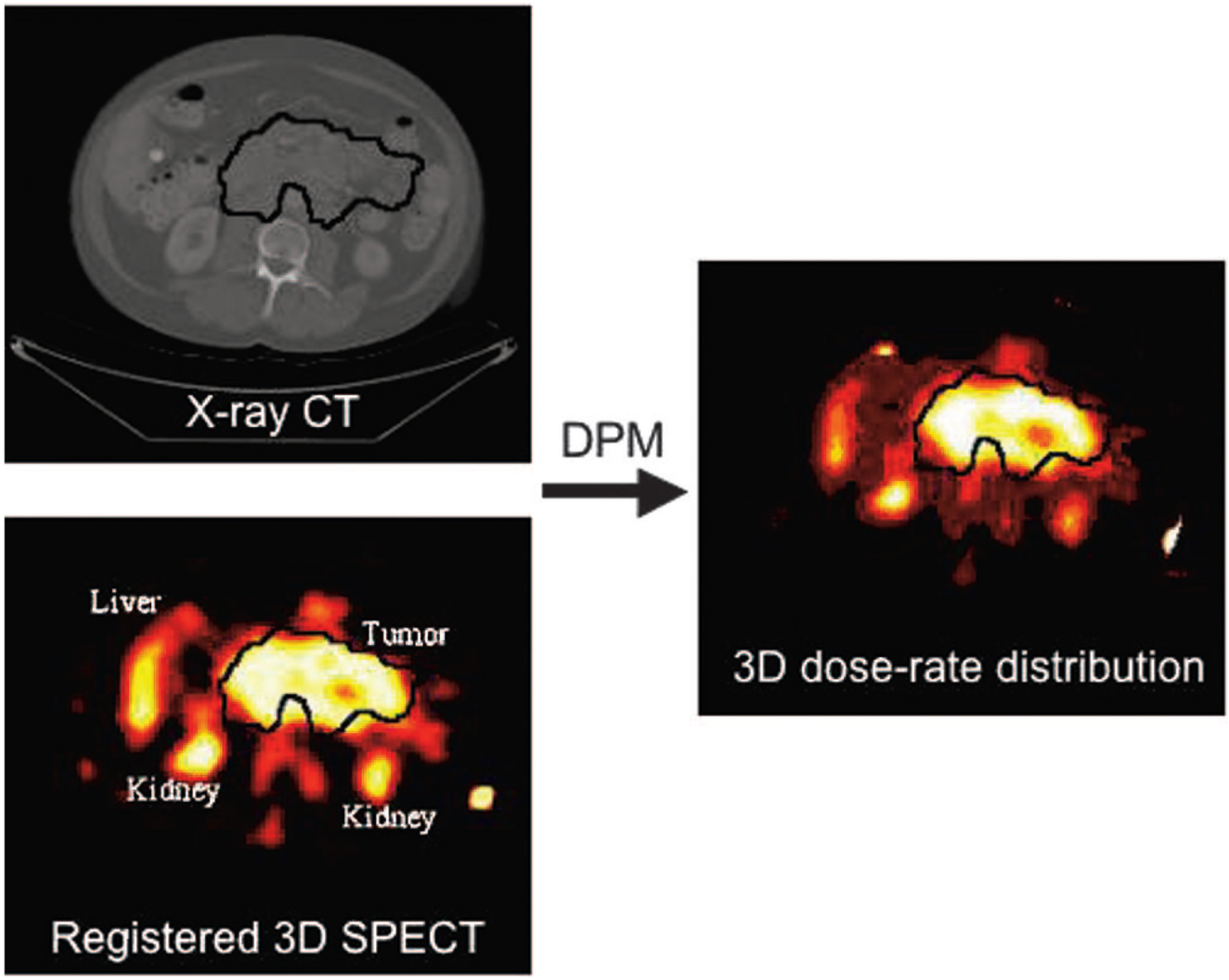

FIGURE 4.
One slice of RIT patient CT image, SPECT image, and corresponding dose-rate map.

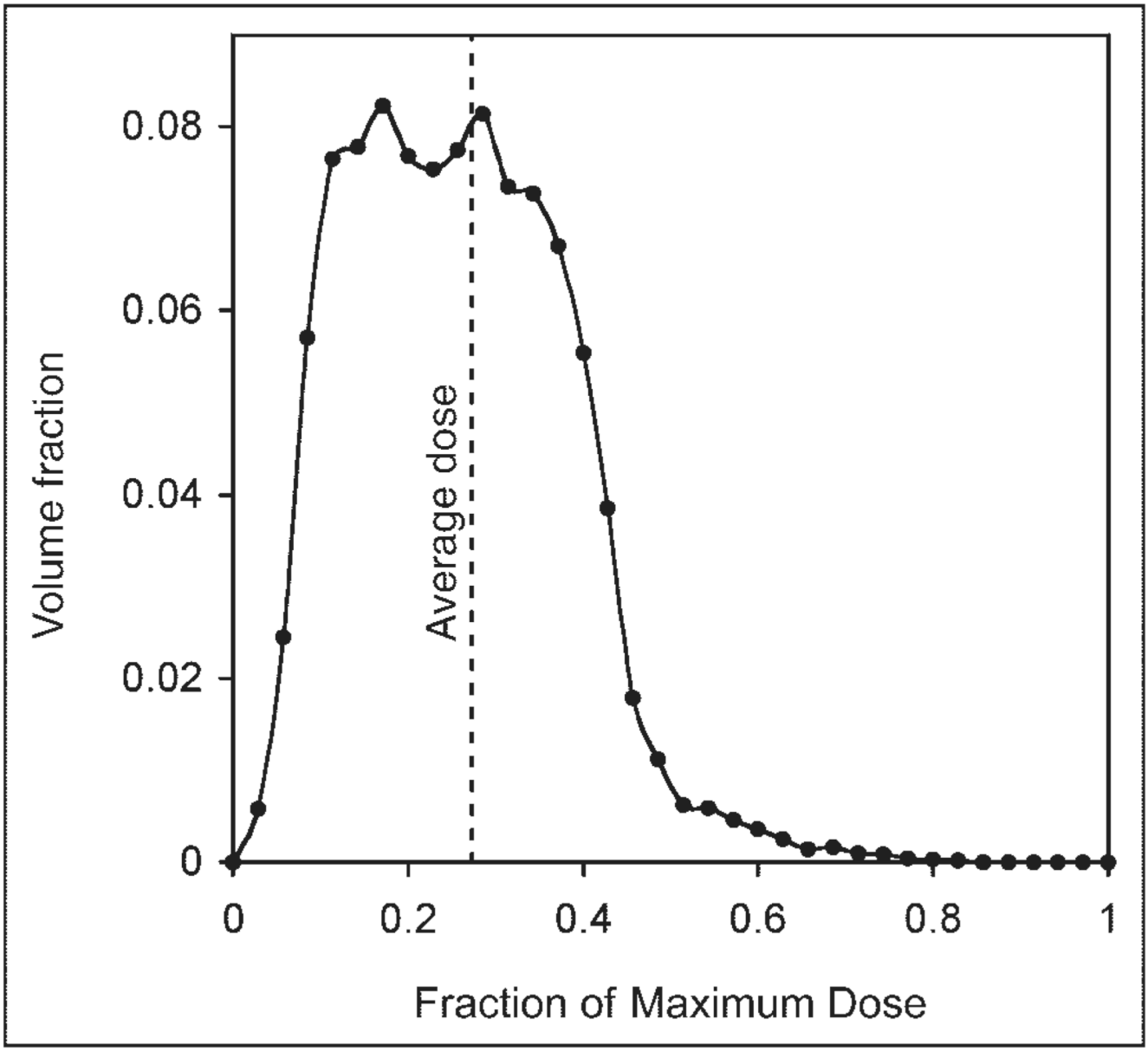

FIGURE 5.
Differential dose-volume histogram corresponding to tumor outlined in patient image of Figure 4.

TABLE 1

Percentage Uptake per Gram Values in 9 Lymphoma Patients Who Underwent ^{131}I RIT at our Clinic

	% uptake/g*						
Patient no.†	**Kidney**	**Liver**	**Lungs**	**Spleen**	**Blood**	**Tumor**	**Whole body**
1	0.0130	0.0047	0.0051	0.0068	0.0084	0.0073	0.0010
3	0.0105	0.0036	0.0040	0.0041	0.0058	0.0079	0.0007
7	0.0124	0.0039	0.0038	0.0069	0.0084	0.0081	0.0010
53	0.0087	0.0025	0.0050	0.0049	0.0086	0.0077	0.0010
75	0.0155	0.0029	0.0069	n/a	0.0116	0.0425	0.0011
73	0.0211	0.0030	0.0056	0.0105	0.0083	0.0128	0.0010
12	0.0124	0.0039	0.0038	0.0069	0.0084	0.0081	0.0010
6	0.0113	0.0036	0.0034	0.0071	0.0060	0.0042	0.0008
23	0.0136	0.0035	0.0037	0.0098	0.0105	0.0503	0.0010

*Percentage uptake relative to total activity administered.

†Patient's identification number.

n/a = data not available.

Values are based on planar imaging 2 d after tracer administration.

TABLE 2

Comparison of ^{131}I S Factors from DPM and the MIRDOSE Program

		S factor (mGy/MBq-s)	
Source	**Target**	**DPM**	**MIRDOSE**
Liver	Liver	2.15E–05*	2.12E–05
Kidney	Kidney	1.19E–04*	1.17E–04
Spleen	Spleen	2.00E–04*	1.93E–04
Liver	Kidney	1.18E–06	8.13E–07
Liver	Spleen	2.71E–07	2.14E–07
Kidney	Liver	1.17E–06	8.13E–07
Kidney	Spleen	1.83E–06	1.85E–06
Spleen	Liver	2.72E–07	2.14E–07
Spleen	Kidney	1.83E–06	1.85E–06

*Adjusted to account for organ mass difference between the Zubal voxel phantom and the Reference Man phantom.

TABLE 3

Calibration Factor (cps/MBq) for 3 Different Calibration Geometries

	Point source: VOI radius					
Collimator	**1 pixel**	**2 pixels**	**3 pixels**	**4 pixels**	**Hot sphere**	**Uniform tank**
HE	7.5	26.2	29.4	29.4	29.1	32.9
UHE	5.5	18.4	20.3	20.3	19.0	19.7

TABLE 4

SPECT Activity Quantification Accuracy (% Error) with Different Calibration Geometries

	Point source calibration							
	VOI radius = 2 pixels		VOI radius = 4 pixels		Hot-sphere calibration		Uniform tank calibration	
Target	**HE**	**UHE**	**HE**	**UHE**	**HE**	**UHE**	**HE**	**UHE**
7-mL tumor	34.3	36.5	41.5	42.4	40.8	38.5	47.7	40.7
16-mL tumor	−0.3	5.1	10.7	13.9	9.6	8.0	20.1	11.4
59-mL tumor	−3.4	7.0	8.0	15.6	6.9	9.9	17.6	13.2
135-mL tumor	−11.7	−4.1	0.5	5.5	−0.6	−0.9	11.0	2.8
Liver	−20.8	−1.1	−7.5	8.3	−8.8	2.0	3.8	5.6
Kidney	−1.8	6.2	9.3	14.8	8.3	9.1	18.9	12.4
Spleen	−12.3	0.1	0.0	9.3	−1.2	3.2	10.5	6.7

TABLE 5

Voxel-Phantom SPECT Activity Quantification Results with HE Collimator and UHE Collimator

Target	True activity (MBq)	SPECT-derived mean activity (MBq)	Relative SD (%)	Error (%)
		HE collimator		
7-mL tumor	2.9	1.6	8.9	43.3
16-mL tumor	6.4	5.7	3.3	10.5
59-mL tumor	23.0	21.4	2.3	6.8
135-mL tumor	52.8	52.9	1.0	−0.2
Liver	205.2	223.1	0.6	−8.8
Kidney	152.5	139.7	0.7	8.4
Spleen	72.5	73.2	0.9	−1.0
		UHE collimator		
7-mL tumor	2.9	1.8	9.4	38.4
16-mL tumor	6.4	5.9	2.2	7.9
59-mL tumor	23.0	20.6	1.2	10.3
135-mL tumor	52.8	53.0	0.9	−0.5
Liver	205.2	200.9	0.4	2.1
Kidney	152.5	138.3	0.5	9.3
Spleen	72.5	70.2	0.7	3.2

TABLE 6

SPECT-Based DPM Results of Mean Absorbed Dose for Targets in Voxel Phantom with HE Collimator and UHE Collimator

Target	True dose (cGy)	SPECT-derived mean dose (cGy)	Relative SD (%)	Error (%)
		HE collimator		
7-mL tumor	1,309	851	7.2	35
16-mL tumor	1,345	1,264	3.0	6
59-mL tumor	1,450	1,431	1.9	1
135-mL tumor	1,458	1,512	0.9	−4
Liver	500	560	0.4	−12
Kidney	1,160	1,128	0.6	3
Spleen	813	859	0.7	−6
		UHE collimator		
7-mL tumor	1,309	898	7.9	31
16-mL tumor	1,345	1,274	1.9	5
59-mL tumor	1,450	1,357	1.0	6
135-mL tumor	1,458	1,493	0.8	−2
Liver	500	502	0.3	0
Kidney	1,160	1,099	0.4	5
Spleen	813	813	0.6	0

TABLE 7

Comparison Between DPM and Conventional Dosimetry Results for the Patient Tumor

Component	Mean tumor absorbed dose (cGy)	
	DPM*	Conventional*
Tumor → tumor	485 (88)	488 (95)
Rest of body → tumor	69 (12)	28 (5)
Total	554	516

*Values in parentheses are percentage.